Dynamical Properties of Sea Surface Microwave Backscatter at Low-Incidence: Correlation Time and Doppler Shift

Olivier Boisot, Laiba Amarouche, Jean-Claude Lalaurie, Charles-Antoine Guérin

Dynamical Properties of Sea Surface Microwave Backscatter at Low-Incidence: Correlation Time and Doppler Shift

Olivier Boisot, Laïba Amarouche, Jean-Claude Lalaurie, and Charles-Antoine Guérin

***Abstract*—We investigate some temporal properties of the microwave backscattered field from the sea surface at low incidence, namely, the decorrelation time and the Doppler shift distribution. These quantities may have an important impact on the performances of the altimeter and synthetic aperture radar systems in Ku- and Ka-bands and must be accurately evaluated. In the framework of classical analytical scattering models and for realistic sea spectra, we obtain a simple expression for the decorrelation time with respect to the main sea state parameters and the scattering geometry. We further propose an original approach based on a time-domain estimator to evaluate the distribution of instantaneous Doppler shifts and the Doppler centroid. The evolution of the latter with the sea state and scattering angles is calculated and discussed. A procedure is proposed to recover the full two-sided Doppler spectrum. We discuss the use of the Doppler shift in view of the geophysical parameter retrieval at low incidence. We find that the surface wind vector can, in principle, be well estimated from the azimuthal variation of the Doppler shift, whereas the signature of the surface current is not sufficient to allow for its estimation.**

***Index Terms*—Correlation time, Doppler shift, low-incidence, microwave ocean remote sensing.**

I. Introduction

IN THE last years, there has been a significant improvement of the capabilities of current or forthcoming altimeter missions in terms of resolution and accuracy. Some of these improvements consist in the replacement of the usual centimeter radar wavelength (C- and Ku-bands) with millimeter wavelength (Ka-band). In a conventional altimeter, such as the AltiKa mission, the use of the Ka-band allows to work at higher pulse repetition frequencies (PRFs) due to the faster decorrelation of the backscattered signal and therefore to reach an average waveform within a smaller amount of time with a correct speckle noise amplitude. In the wide-swath altimetry based on the synthetic aperture radar (SAR) interferometry such as in the Surface Water and Ocean Topography (SWOT) mission concept, Doppler information due to the satellite motion is used to enhance the along-track resolution as it is done in SAR imaging. However, this useful Doppler quantity is affected by a Doppler anomaly due to the motion of waves. The impact of this Doppler anomaly becomes crucial to estimate, as it can impact the SAR ground cells estimated location and azimuthal resolution and, hence, the final geophysical surface estimates. In this respect, the dynamical aspects of the near-nadir backscattered field become crucial, and their impact must be carefully quantified.

There has been a certain number of studies devoted to the analysis of the Doppler signal of the microwave radar echo in the framework of analytic (e.g., [1]–[11]) and rigorous numerical scattering models (e.g., [12]–[18]). As shown in some of these works at large and grazing incidence, a relevant description of the different mechanisms at the origin of the Doppler spectrum requires a (at least weakly) nonlinear description of water waves combined with advanced scattering models that can take into account complex effects related to polarization, multiple scattering, or shadowing. At low incidence, however, the situation is much simpler since the physical optics (PO) is the reference scattering model, whereas nonlinear interactions at the surface can be neglected in the first place. This opens the way to a complete analytic description of the Doppler spectrum in view of further comparisons with experimental data.

In this paper, we propose a study of the correlation time, as well as the Doppler shift of the backscattered signal induced by wave motion at low incidence. We obtain a simple expression of the decorrelation time with respect to the main oceanic parameters. We further discuss the wave-induced Doppler shift and propose an original approach to calculate the Doppler centroid and the full two-sided Doppler spectrum, which is based on the distribution of the instantaneous Doppler shift.

II. Time-Evolving Linear Water Surface

We assume that the elevation of the sea surface about its mean plane is described by a function $z = \eta(\mathbf{r}, t)$ of the horizontal coordinate ($\mathbf{r} = (x, y)$). We adopt the classical linear picture in which the time-evolving sea surface can be written as a continuous summation of independent harmonics, i.e.,

$$\eta(\mathbf{r}, t) = \mathrm{Re}\left\{ \int_{\mathbb{R}^2} a(\mathbf{k}) e^{i(\mathbf{k}\cdot\mathbf{r} - \omega_{\mathbf{k}} t)} d\mathbf{k} \right\} \quad (1)$$

Manuscript received May 25, 2016; revised July 22, 2016; accepted July 22, 2016. This work was supported in part by the Centre National d'Études Spatiales and in part by the Collecte Localisation Satellite.

O. Boisot is with the Mediterranean Institute of Oceanography, University Toulon, Aix Marseille University, CNRS, IRD, MIO UM 110 La Garde, France, and also with the Office National d'Etudes et de Recherches Aérospatiales (ONERA), Salon-de-Provence, France (e-mail: olivier.boisot@univ-tln.fr).

L. Amarouche and J.-C. Lalaurie are with Collecte Localisation Satellite and Centre National d'Études Spatiales, 31400 Toulouse, France (e-mail: lamarouche@cls.fr; Jean-Claude.Lalaurie@cnes.fr).

C.-A. Guérin is with the Mediterranean Institute of Oceanography, University Toulon, Aix Marseille University, CNRS, IRD, MIO UM 110 La Garde, France (e-mail: guerin@univ-tln.fr).

Color versions of one or more of the figures in this paper are available online at http://ieeexplore.ieee.org.

Digital Object Identifier 10.1109/TGRS.2016.2601242

where $a(\mathbf{k})$ is the random complex amplitude of the wave associated to wavenumber $\mathbf{k}$; $\omega_k = \sqrt{g\|\mathbf{k}\| + \gamma_0\|\mathbf{k}\|^3}$ is the gravity–capillarity wave dispersion relationship with $g = 9.81\ \mathrm{m}\cdot\mathrm{s}^{-2}$, i.e., the gravitational constant; and $\gamma_0 = 7.29 \times 10^{-5}\ \mathrm{m}^3\cdot\mathrm{s}^{-2}$, i.e., the surface tension coefficient of seawater (estimated from [19] with a sea surface temperature of 10 °C and a salinity of 35 PSU). The spatiotemporal surface correlation function ($\rho(\mathbf{r},t) = \langle\eta(\mathbf{r},t)\eta(\mathbf{0},0)\rangle$, where $\langle\cdot\rangle$ represents the ensemble average) can be written as

$$\rho(\mathbf{r},t) = \mathrm{Re}\left\{\int_{\mathbb{R}^2} \Psi(\mathbf{k}) e^{i(\mathbf{k}\cdot\mathbf{r}-\omega_\mathbf{k} t)} d\mathbf{k}\right\} \tag{2}$$

where $\Psi(\mathbf{k}) = (1/2)\langle|a(\mathbf{k})|^2\rangle$ is the directional wavenumber spectrum. The latter is usually written in polar coordinates (k,ϕ_k) as

$$\Psi(\mathbf{k}) = \frac{\Psi_0(k)}{k} F(k,\phi_k) \tag{3}$$

where $\Psi_0(k)$ is the omnidirectional spectrum, and $F(k,\phi_k)$ is the spreading function describing the azimuthal variation of wave energy with respect to the wind direction. The directional spectrum is, in general, not centrosymmetric (i.e., $\Psi(-\mathbf{k}) \neq \Psi(\mathbf{k})$) as waves propagating along or against the main wind direction do not have the same energy. However, the spatial variations of a frozen surface at a given time, for example, $t = 0$, are described by a "true" power spectrum, which is the symmetrized version of the directional spectrum, i.e., $\Psi_s(\mathbf{k}) = (1/2)(\Psi(\mathbf{k}) + \Psi(-\mathbf{k}))$. The symmetrized spectrum Ψ_s is relevant for the evaluation of the normalized radar cross section (NRCS) using the classical backscattering model. A popular model is the Elfouhaily *et al.* unified spectrum [20], whose spreading function is described by a simple biharmonic function, i.e.,

$$F(k,\phi_k) = \frac{1}{2\pi}\left\{1 + \Delta(k)\cos\left[2(\phi_k - \phi_w)\right]\right\} \tag{4}$$

where $0 < \Delta(k) < 1$ is a contrast function ensuring a correct ratio of upwind/crosswind slopes, and ϕ_w is the direction of the wind vector with respect to the x-axis. However, such directional spectrum, which does not distinguish the upwind and downwind directions, is insufficient to describe the dynamics of waves. Asymmetric spreading functions have been first proposed by Longuet-Higgins *et al.* [21] and later on refined by Plant [22] in order to preserve the ratio of upwind/crosswind slopes, i.e.,

$$F(k,\phi_k) = \frac{\left[\cos\left(\frac{\phi_k-\phi_w}{2}\right)\right]^{2\gamma(k)}}{\int_{-\pi}^{\pi}\left[\cos\left(\frac{\phi_k-\phi_w}{2}\right)\right]^{2\gamma(k)} d\phi_k} \tag{5}$$

where

$$\gamma(k) = -\ln\left(\frac{1-\Delta(k)}{1+\Delta(k)}\right)\Big/\ln 2. \tag{6}$$

Along this paper, we will adopt this formulation of the spreading function together with the omnidirectional expression of the Elfouhaily *et al.* spectrum in the numerical experiments.

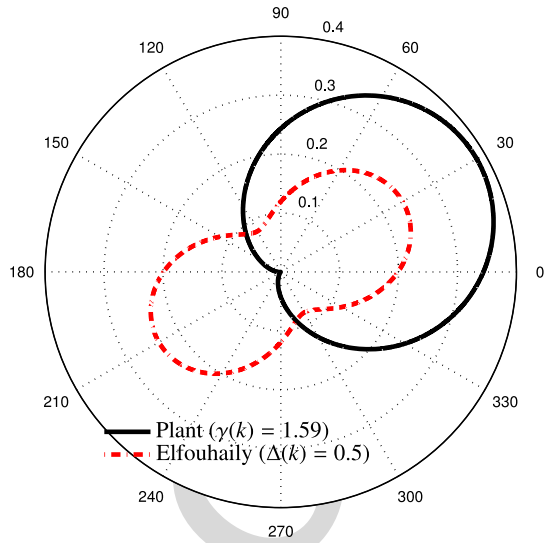

Fig. 1. Comparison of the Elfouhaily 1997 and Plant 2002 spreading functions for $\Delta(k) = 0.5 \leftrightarrow \gamma(k) = 1.59$. In this example, the wind is oriented at 30° from the origin. The dashed circles represent the values of the spreading functions F.

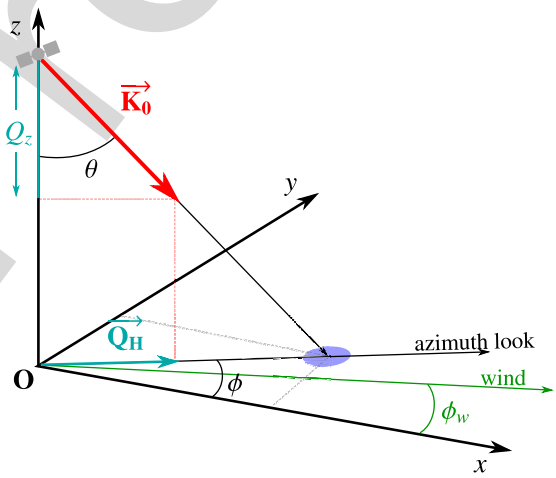

Fig. 2. Schematic of the scattering geometry.

III. Temporal Field Correlation

A. PO Formalism

As it is customary, we assume the incident field on the sea surface to be a monochromatic plane wave with wave vector $\mathbf{K_0}$ and wavenumber K_0 (see Fig. 1). The temporal signal recorded on the receiver is proportional to the complex scattering amplitude $\mathbb{S}(t)$ of the backscattered field (see, e.g., [23]). The backscattered amplitude in the PO approximation, which is also known as the Kirchhoff approximation [24], is given by

$$\mathbb{S}(t) = \frac{1}{(2\pi)^2}\frac{\mathcal{K}}{Q_z}\int_{\mathbb{R}^2} e^{-i\mathbf{Q_H}\cdot\mathbf{r}} e^{iQ_z\eta(\mathbf{r},t)} d\mathbf{r} \tag{7}$$

where we have introduced the so-called Ewald vector $\mathbf{Q} = -2\mathbf{K_0}$ with its horizontal projection $\mathbf{Q_H}$ and vertical projection Q_z, and $\mathcal{K} = \mathbf{Q}^2\mathcal{R}/2$ is a geometric kernel, where $\mathcal{R}$ stands for the complex Fresnel reflection coefficient at normal incidence for sea water. Fig. 2 depicts the geometry of the problem.

The Cartesian system (x, y, z) is a fixed reference frame. The incidence (θ) and azimuth (ϕ) scattering angles are taken with respect to the z- and x-axis, respectively. The azimuthal wind direction is denoted by ϕ_w. In this configuration, the classical observation directions, namely, upwind, crosswind, and downwind, are obtained for the azimuthal angles $\phi = \phi_w \pm \pi$, $\phi = \phi_w \pm \pi/2$, and $\phi = \phi_w$, respectively. The dependence of the viewing angles in expression (7) is implicit. Under the assumption of a Gaussian random process for the sea surface, the resulting field correlation function is given by

$$\begin{aligned} C_{\mathrm{PO}}(t) &= \lim_{A\to\infty} \frac{4\pi}{A} \left(\langle \mathbb{S}(t)\mathbb{S}^*(0)\rangle - |\langle \mathbb{S}(0)\rangle|^2 \right) \\ &= \frac{1}{\pi}\frac{|\mathcal{K}|^2}{Q_z^2} \int\limits_{\mathbb{R}^2} e^{-i\mathbf{Q_H}\cdot\mathbf{r}} \left[e^{-Q_z^2[\rho_0 - \rho(\mathbf{r},t)]} - e^{-Q_z^2\rho_0} \right] d\mathbf{r} \end{aligned} \tag{8}$$

where ρ_0 denotes the surface correlation at the origin (in time and space). Note that the field correlation at the origin, i.e., $C_{\mathrm{PO}}(0)$, reduces to the well-known expression of the NRCS in the Kirchhoff approximation, i.e., σ^0_{PO}. However, the numerical evaluation of this correlation is, in general, more difficult than the ordinary NRCS and deserves a specific numerical procedure using polar coordinates and azimuthal Fourier series expansion.

B. GO Formalism

A well-known approximation of the PO, which is valid in the limit of short radar wavelength, is the geometrical optics (GO) approximation. Simple algebra using a spatiotemporal second-order Taylor expansion of the surface autocorrelation function ρ in the integrand (8) leads to the following expression for the field correlation function in the GO approximation (see the Appendix for detailed calculations):

$$C_{\mathrm{GO}}(t) = \sigma^0_{\mathrm{GO}} \times T_{\mathrm{GO}}(t) \times \mathbb{M}_{\mathrm{GO}}(t). \tag{9}$$

Here, σ^0_{GO} is the classical expression of the NRCS in the GO approximation, i.e.,

$$\begin{aligned} \sigma^0_{\mathrm{GO}} = \frac{|\mathcal{R}|^2}{2\Sigma\cos^4\theta} \exp\Bigg(-\frac{\tan^2\theta}{2\Sigma^2} \big(& s_{yy}^2\cos^2\phi \\ & - 2s_{xy}^2\sin\phi\cos\phi + s_{xx}^2\sin^2\phi \big) \Bigg) \end{aligned} \tag{10}$$

with the directional mean-square slopes (the derivatives are taken at the origin)

$$s_{xx}^2 = -\frac{\partial^2\rho}{\partial x^2},\ s_{yy}^2 = -\frac{\partial^2\rho}{\partial y^2},\ s_{xy}^2 = -\frac{\partial^2\rho}{\partial x \partial_y} \tag{11}$$

$$\Sigma^2 = s_{xx}^2 s_{yy}^2 - s_{xy}^4. \tag{12}$$

The second term T_{GO} is a Gaussian damping function, i.e.,

$$T_{\mathrm{GO}}(t) = \exp\left(-2K_0^2 L^2 \cos^2\theta\, t^2\right) \tag{13}$$

with

$$L^2 = s_{tt}^2 - \frac{s_{yy}^2 s_{xt}^2 - 2s_{xy}^2 s_{xt} s_{yt} + s_{xx}^2 s_{yt}^2}{\Sigma^2} \tag{14}$$

$$s_{tt}^2 = -\frac{\partial^2\rho}{\partial t^2}, s_{xt} = \frac{\partial^2\rho}{\partial x \partial t},\ s_{yt} = \frac{\partial^2\rho}{\partial y \partial t}. \tag{15}$$

The second-order time derivative s_{tt}^2 can be interpreted as the variance of the vertical orbital velocity of waves. The spatiotemporal cross-derivatives s_{xt} and s_{yt} have no such simple interpretation. The third term in (9) is a complex azimuthal modulation function, i.e.,

$$\begin{aligned} \mathbb{M}_{\mathrm{GO}}(t) = \exp\Bigg(& -i\frac{2K_0 t}{\Sigma^2}\sin\theta \\ & \times \left[\left(s_{yy}^2 s_{xt} - s_{xy}^2 s_{yt} \right)\cos\phi + \left(s_{xx}^2 s_{yt} - s_{xy}^2 s_{xt} \right)\sin\phi \right] \Bigg). \end{aligned} \tag{16}$$

Note that the expression of the temporal correlation in the GO framework solely depends on the spatiotemporal second-order derivatives of the surface correlation function at the origin. These coefficients can be easily obtained using the corresponding moments of the power spectrum.

C. Correlation Time

The correlation time τ_c of the backscattered field is typically defined by

$$|C(\tau_c)| = a\, C(0) \tag{17}$$

where $|\cdot|$ stands for the absolute value (modulus), for some threshold $0 < a < 1$. This quantity must be numerically evaluated in the PO formalism but can be analytically estimated in the GO formalism, with $T_{\mathrm{GO}}(\tau_c) = a$, yielding

$$\tau_c = \frac{\sqrt{-\ln(a)/2}}{K_0|\cos\theta| L}. \tag{18}$$

Note that the correlation time does not depend on the azimuth angle in the GO formalism, which is confirmed by numerically calculating this correlation time with the PO formalism. Moreover, we numerically found that the correlation times calculated from the PO formalism and from the GO formalism are very close in Ku- and Ka-bands, although the corresponding NRCS can be significantly different (i.e., the GO formalism is not valid to evaluate the NRCS at low incidence but useful to evaluate the correlation time). At an incidence angle of $\theta = 20°$, which is in the limit of validity of the models, we found an absolute difference smaller than 0.1 ms between the PO and GO correlation times.

The simple analytic expression (18) of the correlation time shows that the field decorrelation is mainly due to the motion of the wave field in the line-of-sight of the radar through the vertical orbital wave velocity (s_{tt}^2), which is numerically found to be the dominant term in (14), i.e., $L \simeq s_{tt}$. This quantity is related to the first moment of the wave spectrum and is mainly contributed to by long waves, i.e.,

$$s_{tt}^2 = \int\limits_0^\infty \omega_k^2 \Psi_0(k) dk \simeq g \int\limits_0^\infty k \Psi_0(k) dk. \tag{19}$$

For wind waves spectra in the gravity range, i.e., $\Psi_0(k) \sim k^{-3}$ and $s_{tt}^2 \simeq g k_p H_s^2/8$, where k_p is the peak wavenumber. Hence,

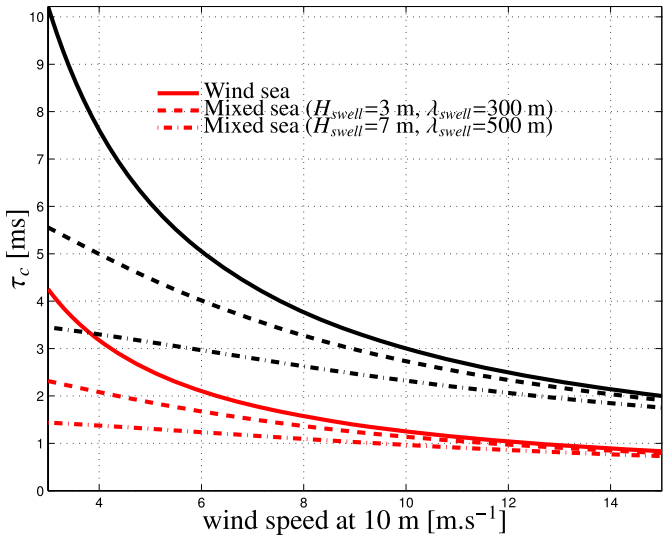

Fig. 3. Correlation time τ_c in (red lines) Ka-band ($f_0 = 36$ GHz) and (black lines) Ku-band ($f_0 = 15$ GHz) at nadir as a function of wind speed at 10 m for the decorrelation threshold $a = 1/e$.

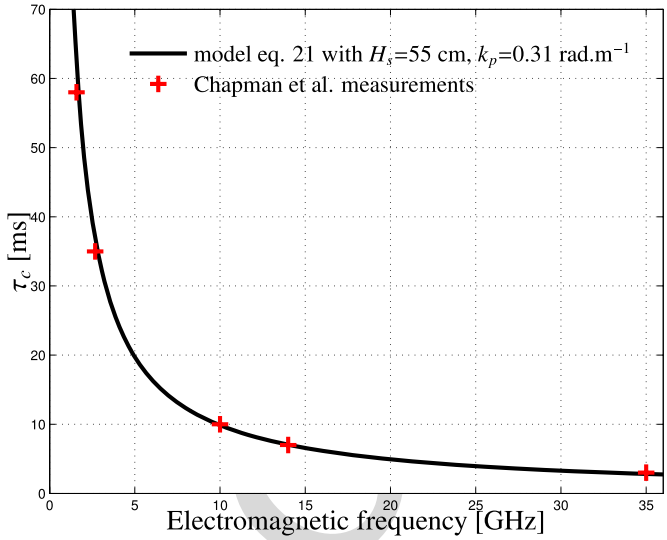

Fig. 4. Comparison of the correlation time according to model (20) and Chapman *et al.* [25] measurements as a function of the electromagnetic frequency at nadir for a decorrelation threshold $a = 1/\mathrm{e}$.

the correlation time can be simply expressed in terms of the main oceanic parameters k_p and H_s, i.e.,

$$\tau_c \simeq \frac{2\sqrt{-\ln(a)}}{K_0|\cos\theta|\sqrt{gk_p}H_s}. \tag{20}$$

In the case of a mixed sea composed of a swell (with wavenumber k_{swell} and significant wave height H_{swell}) and a wind sea (with peak wavenumber k_p and significant wave height H_{wind}, the aforementioned formula can be easily adapted with $s_{tt}^2 \simeq gk_pH_{\mathrm{wind}}^2/8 + gk_{\mathrm{swell}}H_{\mathrm{swell}}^2/16$.

Fig. 3 shows a comparison of the correlation time τ_c in Ku- (15 GHz) and Ka-band (36 GHz) at nadir as a function of wind speed at 10 m above the sea surface, with a decorrelation threshold set to $a = 1/e$. It has been calculated with both the GO-based formula (18) and the PO model, with no numerical difference. In addition to a pure wind sea case, a mixed sea with a swell of wavelength longer than the dominant wind sea wavelength (for a 15 m $\cdot$ s^{-}1 wind speed, the dominant wavelength is about 200 m) has been considered. For a pure wind sea, the correlation time is decreased by a factor 4–5 from low to high wind speed. In the case of a mixed sea, the correlation time is less sensitive to the wind speed and is mainly driven by the swell parameters. It ranges from 0.5 to 4 ms in Ka-band and from 2 to 10 ms in Ku-band. The simplified expression (20) for the correlation time has been compared with expression (18) and is found in excellent agreement (with at most a few percent relative difference), showing that the correlation time can be expressed in a simple and accurate manner with only the peak wavenumber and the significant wave height.

A study of the phase of the backscattered signal from the sea surface has been conducted by Chapman *et al.* [25], where authors give measurements of the backscattered signal correlation time at nadir for different microwave frequencies. Results are given for a developed sea with $u_{10} \simeq 4.7$ m/s with negligible swell. Using the classical relation for fully developed wind seas, i.e., $H_s = 0.025 \times u_{10}^2$ and $k_p = 0.84^2 g/u_{10}^2$, we obtain $k_p \simeq 0.31$ rad $\cdot$ m^{-1} and $H_s \simeq 55$ cm. Fig. 4 compares the measurements of the decorrelation time by Chapman *et al.* and the estimation after formula (20) as a function of radar frequency. An excellent agreement is obtained.

IV. Wave-Induced Doppler Shift

A. Different Approaches to the Doppler Centroid

As it is well known, the backscattered time signal undergoes a Doppler shift due to the combined motion of the platform (airborne or spaceborne sensor) and the motion of waves at the sea surface. The dominant contribution to the Doppler centroid frequency arises from the relative velocity of the platform with respect to the ground. It can be easily estimated and removed by means of a geometrical model. The residual Doppler shift, or Doppler anomaly, due to wave motion is much smaller but induces azimuthal smearing resulting in the loss of resolution in the SAR image. Here, we will try to estimate its statistical properties as a function of sea state. There are several approaches to calculate the Doppler shift of waves. The most classical technique is the frequency-domain estimation (FDE) based on the Doppler spectrum. For this, the Fourier transform of the temporal correlation function is taken, i.e.,

$$D(f) = \int_{-\infty}^{+\infty} e^{-2i\pi ft} C(t) dt \tag{21}$$

and the Doppler shift is defined as the mean (e.g., [7] and [8]) or median (see [26]) frequency with respect to the normalized distribution $D(f)/\int D(f)df$. In practice, the Doppler spectrum $D(f)$ is obtained through the variance of the periodogram of the time signal (i.e., the sample average of $|\mathrm{FFT}(\mathbb{S}(t))|^2$). The advantage of the technique is that it gives the full shape of the Doppler spectrum and discriminate positive and negative frequency shifts ($D(-f) \neq D(f)$, in general). Note that the estimation of the Doppler shift based on the mean or median of

the Doppler spectrum is meaningful only if the latter is essentially half-sided, as the negative and frequency components of the two-sided spectrum would cancel out and make the mean Doppler shift actually close to zero. The difficulty of the technique for simulation purposes is the full calculation of the temporal correlation function necessary to estimate the Doppler spectrum. To avoid this calculation, one often limits oneself to the estimation of the first two moments of the Doppler spectrum, which can be obtained with the time derivative of the signal correlation function at the origin (see, e.g., [7] and [8]).

Another approach is the time-domain estimator (TDE), which has been found advantageous in the context of SAR systems (see [26]). It consists in estimating the phase of the complex signal correlation, i.e.,

$$C(t) = |C(t)|\, e^{i2\pi t f_c}. \tag{22}$$

The mean Doppler shift frequency is then simply obtained with

$$f_c = \frac{1}{t} \arg\left(C(t)\right). \tag{23}$$

This approach (also employed in [6] in the context of analytic scattering models) has the merits of simplicity but does not provide the dispersion around the Doppler shift.

An alternative TDE can be obtained using the instantaneous random signal, $\mathbb{S}(t)$ instead of its correlation function. We define the instantaneous Doppler frequency shift induced by wave motion as

$$f(t) = -\frac{1}{2\pi}\partial_t \varphi(t) \tag{24}$$

where $\varphi(t)$ is the scattering phase of the illuminated target (we note that with this convention, positive frequencies represent waves traveling to the radar). The scattering phase is related to the complex backscattered signal $\mathbb{S}(t)$ through

$$\varphi(t) = \arg\left(\mathbb{S}(t)\right) = \arctan\left[\frac{\mathrm{Im}\left(\mathbb{S}(t)\right)}{\mathrm{Re}\left(\mathbb{S}(t)\right)}\right] \tag{25}$$

from which we can infer the simple expression

$$f(t) = -\frac{1}{2\pi}\mathrm{Im}\left[\frac{\partial_t \mathbb{S}(t)}{\mathbb{S}(t)}\right]. \tag{26}$$

We define the instantaneous Doppler shift distribution as the probability density function (pdf) associated to this last quantity.

B. Doppler Shift in the PO Formalism

Using expression (7) of the scattered field in the PO approximation, we obtain

$$f(t) = -\frac{1}{2\pi}\mathrm{Im}\left(\frac{N_t}{D_t}\right) \tag{27}$$

with

$$\begin{cases} N_t = iQ_z \int_{\mathbb{R}^2} \partial_t \eta(\mathbf{r},t) e^{-i\mathbf{Q_H}\cdot\mathbf{r}} e^{iQ_z\eta(\mathbf{r},t)} d\mathbf{r} \\ D_t = \int_{\mathbb{R}^2} e^{-i\mathbf{Q_H}\cdot\mathbf{r}} e^{iQ_z\eta(\mathbf{r},t)} d\mathbf{r}. \end{cases} \tag{28}$$

Here, a common normalization factor $2\pi\sqrt{A}$ appeared in the calculation and vanished to make these quantities independent of the illuminated area A. By virtue of the central limit theorem, these random surface integrals follow a centered complex-normal distribution. Classical two-point calculations on Gaussian random variables lead to the following expressions for their respective co- and cross-variances:

$$\begin{cases} \left\langle |N_t|^2 \right\rangle = -Q_z^2 \int\limits_{\mathbb{R}^2} \left[Q_z^2 \left(\partial_t \rho(\mathbf{r},0)\right)^2 + \partial_{tt}\rho(\mathbf{r},0)\right] \\ \qquad\qquad \times e^{-i\mathbf{Q_H}\cdot\mathbf{r}} e^{-Q_z^2[\rho_0 - \rho(\mathbf{r},0)]} d\mathbf{r} \\ \left\langle |D_t|^2 \right\rangle = \int\limits_{\mathbb{R}^2} e^{-i\mathbf{Q_H}\cdot\mathbf{r}} e^{-Q_z^2[\rho_0-\rho(\mathbf{r},0)]} d\mathbf{r} \\ \left\langle N_t^* D_t \right\rangle = Q_z^2 \int\limits_{\mathbb{R}^2} \partial_t \rho(\mathbf{r},0) e^{-i\mathbf{Q_H}\cdot\mathbf{r}} e^{-Q_z^2[\rho_0-\rho(\mathbf{r},0)]} d\mathbf{r}. \end{cases} \tag{29}$$

Note that these quantities are time independent, with the second term equal to the NRCS in PO approximation, apart from a geometrical factor. The pdf associated to the phase derivative (27) can be obtained using recent results on the ratio of two correlated complex-Gaussian random variables (see [27]). It can be expressed as a nonstandardized Student's t-distribution

$$p(f) = \frac{\pi}{\sqrt{2}\Delta f}\left[1 + \frac{1}{2}\left(\frac{f - f_c}{\Delta f}\right)^2\right]^{-3/2} \tag{30}$$

with the mean (central) Doppler shift frequency

$$f_c = \frac{C_i}{2\pi}\frac{\left\langle |N_t|^2 \right\rangle^{\frac{1}{2}}}{\left\langle |D_t|^2 \right\rangle^{\frac{1}{2}}} \tag{31}$$

and the dispersion parameter

$$(\Delta f)^2 = \frac{1 - |C|^2}{8\pi^2}\frac{\left\langle |N_t|^2 \right\rangle}{\left\langle |D_t|^2 \right\rangle}. \tag{32}$$

It involves the complex cross correlation of the random variables N_t and D_t, i.e.,

$$C = \frac{\left\langle N_t^* D_t \right\rangle}{\sqrt{\left\langle |N_t|^2 \right\rangle \left\langle |D_t|^2 \right\rangle}} \tag{33}$$

which is decomposed into real and imaginary parts, i.e., $C = C_r + iC_i$. From this, we obtain a simple representation of the Doppler shift distribution after (24) requiring only the calculation of the three surface integrals in (29) involved in the three statistical parameters (31)–(33). Note that expression (31) of the mean Doppler shift is consistent with expression [7, eq. (IV.12)] derived from the first moment of the Doppler spectrum obtained with the FDE. Note, however, that the Doppler shift distribution (30) does not possess a finite variance, contrarily to the latter definition. Nevertheless, the nonstandardized Student's t-distribution possesses a dispersion parameter (Δf) allowing to characterize the dispersion around its mean. We performed a numerical calculation of the mean Doppler shift due to wave motion (f_c) and its dispersion (Δf) with the sea spectrum described in Section II. An efficient numerical evaluation of the surface integrals in (29) has been achieved using an integration in polar coordinates together with an azimuthal Fourier expansion of the surface correlation functions

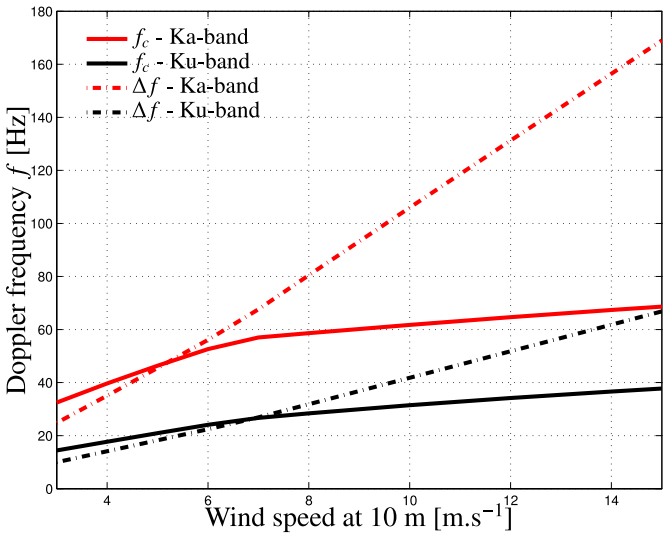

Fig. 5. Evolution of the residual Doppler shift parameters: central frequency f_c (plain) and dispersion parameter Δ_f (dash-dotted) as a function of surface roughness represented with the wind speed at 10 m for an incidence angle $\theta = 5°$ in the upwind direction. Red plots represent the calculation in Ka-band ($f_0 = 36$ GHz), and black plots represent the calculation in Ku-band ($f_0 = 15$ GHz).

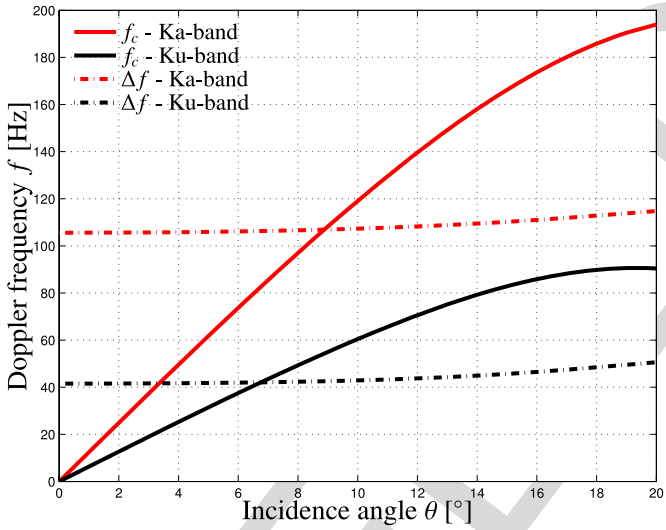

Fig. 6. Same as Fig. 5 except that parameters are plotted as a function of the incidence angle θ for a wind speed at 10 m of 10 m $\cdot$ s^{-1} in the upwind direction.

and related quantities. Figs. 5–7 describe the evolution of the center and width of the Doppler shift distribution as a function of surface roughness (see Fig. 5), incidence angle θ (see Fig. 6), and azimuth angle ϕ (see Fig. 7) for the two microwave bands, i.e., Ka ($f_0 = 36$ GHz) and Ku ($f_0 = 15$ GHz).

The mean and dispersion parameters of the residual Doppler shift have a similar behavior in the two microwave bands, except that absolute values are higher in Ka-band. In our calculations, their ratio between the two bands is found to be nearly constant and about 2 for the central frequency and 2.5 for the dispersion parameter regardless of the scattering geometry and surface roughness. Note that the ratio of the residual Doppler shift central frequencies is close but not equal to the ratio of radar wavelengths (2.4). Fig. 5 shows that the

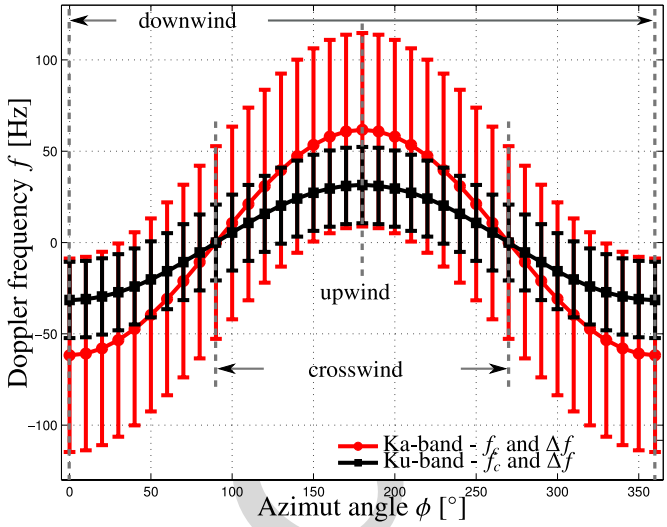

Fig. 7. Same as Fig. 5 except that parameters are plotted as a function of the azimuth angle ϕ for an incidence angle $\theta = 5°$, a wind speed at 10 m of 10 m $\cdot$ s^{-1}, and a wind direction $\phi_w = 0°$. Dispersion parameter Δ_f is plotted as an error bar around its mean f_c.

central frequency f_c has a weak sensitivity to sea state, whereas the dispersion parameter undergoes a dramatic increase with wind speed. Hence, it seems that the width of the Doppler shift distribution is a better proxy for wind speed estimation than its mean value. The situation is opposite when it comes to the dependence on the scattering angles: Fig. 6 shows that central frequency f_c quickly increases with the incidence angle, whereas the dispersion parameter remains quite constant. The same qualitative behavior holds for the azimuthal dependence, with a central frequency oscillating between positive (upwind angular sector) and negative (downwind angular sector) values and a quasi-constant dispersion parameter. A noticeable result is that the central frequency follows a sinusoidal dependence on the azimuthal angle as will be confirmed later on the basis of theoretical considerations (see the discussion in Section VI-A).

V. Two-Sided Doppler Spectrum

Doppler spectra in the microwave regime exhibit, in general, asymmetric components in the positive and negative frequencies related to the velocities of waves traveling to and away from the radar. The previous definition of the instantaneous frequency (27) does not allow to differentiate the progressive and regressive parts of the surface, which separately contributes to the two parts of the Doppler spectrum. Hence, the instantaneous Doppler shift distribution (30) is expected to be consistent with normalized Doppler spectra, according to the classical definition (21) for the one-sided spectra only (i.e., if all waves are supposed to travel in the same direction). To be able to distinguish positive and negative frequencies, we mathematically decompose the surface into a sum of progressive and regressive waves (i.e., waves traveling to or against the radar look direction)

$$\eta(\mathbf{r}, t) = \eta^+(\mathbf{r}, t) + \eta^-(\mathbf{r}, t) \tag{34}$$

where η^+ (respectively, η^-) is defined by the integral (1), with a domain of integration restricted to wave vectors in the same

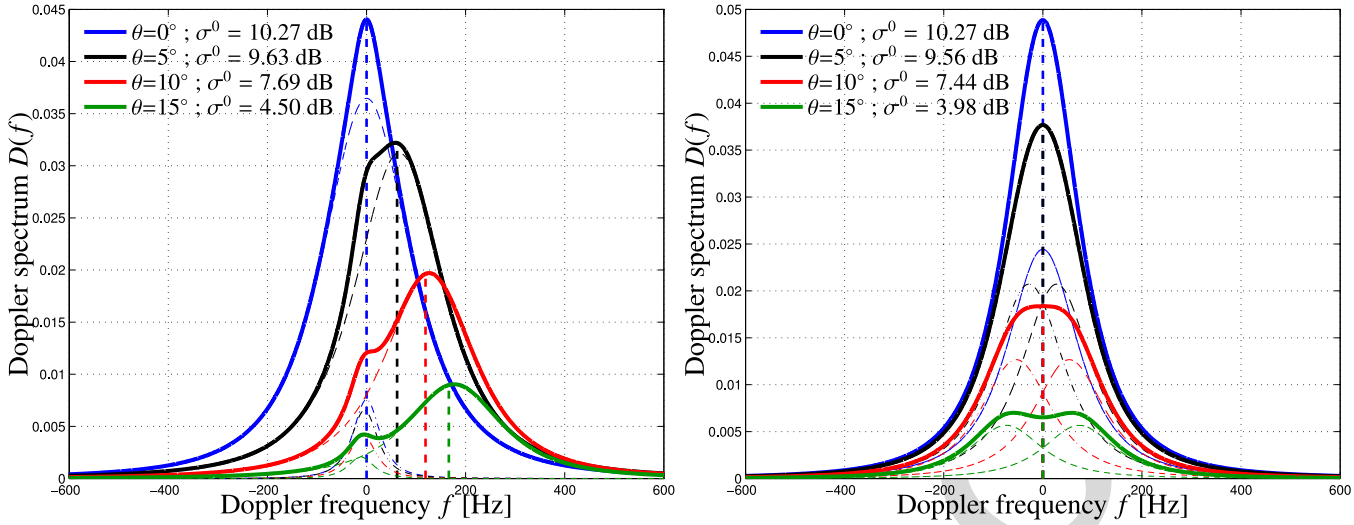

Fig. 8. Examples of the recomposed Doppler spectrum (thick lines) calculated for a wind speed at 10 m of 10 m · s^{-1} in Ka-band ($f_0 = 36$ GHz) and several values of incidence angles θ. (Left) Calculation is made in the upwind direction. (Right) Calculation is made in the crosswind direction. The thin dashed lines represent the progressive part, and the thin dash-dotted lines the regressive part of the Doppler spectrum. The thick dashed lines represent the central frequency of the Doppler shift f_c. AQ6

half-plane (respectively, opposite half-plane) as the radar incident wavenumber, i.e., $\mathbf{K_0} \cdot \mathbf{k} > 0$ (respectively, $\mathbf{K_0} \cdot \mathbf{k} < 0$). We accordingly decompose the surface autocorrelation function with

$$\rho(\mathbf{r}, t) = \rho^+(\mathbf{r}, t) + \rho^-(\mathbf{r}, t) \tag{35}$$

where, analogously, $\rho^\pm$ is defined through the spectral integral (2) restricted to the integration domain $\pm\mathbf{K_0} \cdot \mathbf{k} > 0$. We now assume that the Doppler spectrum is the summation of two subspectra obtained by assuming that only one category of waves is moving (progressive or regressive), whereas the other is frozen. Each subspectrum is proportional to the distribution $p^\pm$ of instantaneous Doppler shifts $f^\pm$ associated to the progressive and regressive parts of the surface, i.e.,

$$f^\pm(t) = -\frac{1}{2\pi}\partial_t\varphi^\pm(t) = -\frac{1}{2\pi}\mathrm{Im}\left[\frac{\partial_t\mathbb{S}^\pm(t)}{\mathbb{S}(t)}\right] \tag{36}$$

where it is understood that the time derivation $\partial_t\mathbb{S}^+$ is taken with respect to the progressive part of the surface only (η^+), the regressive part (η^-) being frozen, and conversely for $\partial_t\mathbb{S}^-$. We can therefore rewrite

$$D(f) = \alpha^+ p^+(f) + \alpha^- p^-(f) \tag{37}$$

AQ5 for some weights $\alpha^\pm$ to be determined. The moments on the order of 0 and 1 of the Doppler spectrum must satisfy the following consistency relation with the NRCS (σ^0) and the mean Doppler shift:

$$\begin{cases} \sigma^0 = \alpha^+ + \alpha^- \\ \sigma^0 f_c = \alpha^+ f_c^+ + \alpha^- f_c^- \end{cases} \tag{38}$$

where f_c and $f_c^\pm$ are the mean frequencies associated to the Doppler spectrum and its subspectra

$$f_c = \int_{\mathbb{R}} f\, p(f) df,\ f_c^\pm = \int_{\mathbb{R}} f\, p^\pm(f) df. \tag{39}$$

By solving this last system of equations, we obtain

$$\alpha^\pm = \pm\sigma^0 \frac{f_c - f_c^\mp}{f_c^+ - f_c^-}. \tag{40}$$

The calculation of the pdf of the phase derivatives ($p^\pm$) in the PO formalism is very similar to the calculation developed in Section IV-B, with the difference that the time derivation should be taken with respect to progressive or regressive waves only. The formula (28)–(33) remain similar with the only change that N_t and related quantities should be replaced by

$$\begin{cases} N_t^\pm = iQ_z \int_{\mathbb{R}^2} \partial_t\eta^\pm(\mathbf{r}, t) e^{-i\mathbf{Q_H}\cdot\mathbf{r}} e^{iQ_z\eta(\mathbf{r},t)} d\mathbf{r} \\ \left\langle |N_t^\pm|^2 \right\rangle = -Q_z^2 \int\limits_{\mathbb{R}^2} \left[Q_z^2 \left(\partial_t\rho^\pm(\mathbf{r}, 0)\right)^2 + \partial_{tt}\rho^\pm(\mathbf{r}, 0) \right] \\ \qquad\qquad \times e^{-i\mathbf{Q_H}\cdot\mathbf{r}} e^{-Q_z^2[\rho_0 - \rho(\mathbf{r},0)]} d\mathbf{r} \\ \left\langle N_t^{\pm *} D_t \right\rangle = Q_z^2 \int\limits_{\mathbb{R}^2} \partial_t\rho^\pm(\mathbf{r}, 0) e^{-i\mathbf{Q_H}\cdot\mathbf{r}} e^{-Q_z^2[\rho_0 - \rho(\mathbf{r},0)]} d\mathbf{r} \end{cases} \tag{41}$$

Fig. 8 shows an example of the two-sided Doppler spectrum in Ka-band at 10 m/s wind speed for different incidence angles. At low incidence, the positive and negative Doppler spectra merged into a single wider peak.

VI. Estimation of Surface Parameters

A. Wind Direction and Doppler Shift

Recent studies with coherent radars have established a clear relationship between the centroid of the Doppler anomaly and the wind vector above the sea surface (e.g., [28]–[31]) at moderate and large incidence angles ($> 20°$). However, at low incidence, the central residual Doppler shift has a weak dynamic with respect to wind speed and is smaller than the dispersion parameter, as shown in Fig. 5. This makes the Doppler anomaly, when taken at fixed angles, a bad tracer for the wind vector. Nevertheless, a clear dependence with wind direction can be seen on the azimuthal variations of the Doppler shift central frequency. The sinusoidal variation observed in Fig. 7 can be well understood using GO-like developments

for the central frequency (31) expressed in the PO formalism. The main advantage of this formulation is that the central frequency is expressed as a function of statistical parameters of the surface and does not depend on the chosen wave spectrum. The expression of the central frequency is the same as the complex azimuthal modulation function of the GO formalism (16) and is expressed, in term of central frequency, i.e.,

$$f_c = -\frac{K_0 \sin\theta}{\pi\Sigma^2}\left[\left(s_{yy}^2 s_{xt} - s_{xy}^2 s_{yt}\right)\cos\phi + \left(s_{xx}^2 s_{yt} - s_{xy}^2 s_{xt}\right)\sin\phi\right] \quad (42)$$

which can be rewritten as

$$f_c = -F_c \cos(\phi - \phi_w) \quad (43)$$

where

$$F_c = \frac{K_0 \sin\theta}{\pi\Sigma^2}\sqrt{\left(s_{yy}^2 s_{xt} - s_{xy}^2 s_{yt}\right)^2 + \left(s_{xx}^2 s_{yt} - s_{xy}^2 s_{xt}\right)^2} \quad (44)$$

is the maximum central frequency, and

$$\tan(\phi_w) = \frac{s_{xx}^2 s_{yt} - s_{xy}^2 s_{xt}}{s_{yy}^2 s_{xt} - s_{xy}^2 s_{yt}} \quad (45)$$

is the wind direction. The approximate formulas (42)–(45) based on GO-like expansion therefore explains the observed sinusoidal variation with the azimuthal angle observed in the PO formalism. However, they are not accurate enough to reproduce the full dependence on the incidence angle. For example, it is shown in Fig. 6 that the evolution with the incidence angle is not merely sinusoidal as suggested by (44), although it is a good approximation at the lowest angles. This loss of accuracy in using the GO-like expression of the central frequency mainly arises from the difference between the PO and GO models in estimating the NRCS. As it is well known, the GO model has a more restricted domain of validity than the PO as the incidence angle is increased. Since the signal intensity enters in the calculation of the central frequency (see parameter $\langle |D_t|^2 \rangle$ in (29) which is proportional to the NRCS), this explains the slight discrepancy of the mean Doppler shifts calculated after these two models at a higher incidence. Note that this is not the case for the correlation time estimated in Section III, which is robust to the use of the GO model since it involves only the normalized (i.e., divided by the NRCS) spatiotemporal correlation function of the backscattered signal. An interesting consequence of the sinusoidal variation in azimuth for the central frequency is that a robust joint estimator of both the wind direction (ϕ_w), and the maximum central frequency (F_c) can be built from any azimuthal sampling of the instantaneous residual Doppler shift at a fixed incidence angle. This could be achieved, for example, using a maximum-likelihood estimator, as was done in [32] in the context of NRCS azimuthal airborne data with a strong level of noise. However, the construction and evaluation of this estimator goes beyond the scope of this paper and is left for further research.

B. Influence of a Constant Surface Drift

In the last decade, it has been demonstrated with spaceborne [5] and airborne [30] data that the Doppler shift of the radar echo carries a clear signature of the surface current once corrected from the wind–wave-induced Doppler anomaly. These results are, however, limited to medium incidences and strong currents, and we will address here the issue of low incidence and small currents. The additional Doppler frequency shift induced by a surface drift of norm U oriented in the horizontal plane with an azimuth angle ϕ_U with respect to the x-axis (see Fig. 2) is of the form

$$f_{\text{drift}} = -\frac{2}{\lambda_0} U \sin\theta \cos(\phi - \phi_U) = -F_U \cos(\phi - \phi_U). \quad (46)$$

The resulting total Doppler shift is given by (assuming no hydrodynamical interactions between surface drift and wave motion)

$$F = -F_c \cos(\phi - \phi_w) - F_U \cos(\phi - \phi_U) = -F_m \cos(\phi - \Phi) \quad (47)$$

where F_m and Φ are a combination of the Doppler shift parameters associated to wave motion and surface drift

$$\begin{cases} F_m = \sqrt{F_c^2 + F_U^2 + 2F_c F_U \cos(\phi_w - \phi_U)} \\ \tan\Phi = \frac{F_c \sin\phi_w + F_U \sin\phi_U}{F_c \cos\phi_w + F_U \cos\phi_U}. \end{cases} \quad (48)$$

The four unknown parameters $F_C, F_U, \phi_w,$ and ϕ_U cannot be recovered from the sole knowledge of F_m and Φ. Therefore, the inversion of the surface current magnitude and direction requires independent knowledge and compensation of the wave-induced surface velocity, as was done in [30] with the airborne ATI SAR data. Furthermore, even in the most favorable case, where the surface drift is oriented in the direction of the azimuthal look of the radar ($\phi_U = \phi$), we find $F_U/F_c \simeq 0.4\ \text{s}\cdot\text{m}^{-1}\ U$ in Ka-band and $\simeq 0.3\ \text{s}\cdot\text{m}^{-1}\ U$ in Ku-band at $10\ \text{m}\cdot\text{s}^{-1}$ wind speed, regardless of the incidence angle. Hence, given the level of dispersion of the residual Doppler shift, the relative variation induced by the surface drift seems too small (4% for $U = 10\ \text{cm}\cdot\text{s}^{-1}$) to allow for an estimation of the latter in the case of moderate small-scale surface currents, even if the wave-induced Doppler anomaly is known from some other instrument or a geophysical model function (such as [28]).

C. Potential Applications to Forthcoming Spaceborne Missions

This study was primarily motivated by the need to estimate the loss of resolution and ground cells shifts induced by wave motion for the SWOT Ka interferometer (Karin, [33]). In its Low Rate mode over the ocean surface, the nominal resolution is expected to be 1 km^2 after averaging of the 250-m on-board unfocused SAR resolution at a PRF of 4420 Hz with 2-ms integration time. Our analysis has shown that with such a value, the integration time remains larger than the correlation time, which has been found on the order of 1 ms so that the multilook averaging process is efficient in processing independent samples.

However, the wave-induced Doppler shifts are not negligible and have to be considered in the algorithms used to estimate ocean surface parameters from on-board radar altimeter signals.

Indeed, if we consider the configuration of SWOT mission and, for example, an incidence angle of 3° in the upwind direction for a wind speed of 10 $\mathrm{m} \cdot \mathrm{s}^{-1}$ at 10 m, the mean Doppler shift is of 40 Hz (see Fig. 6). This Doppler shift, if not corrected for, induces a shift of the ground cells location of about 20 m (using a simple relationship between Doppler frequency and ground location), which may be not negligible for the ocean height estimation.

In the case of crosswind direction, the mean Doppler shift was found to be zero. Nevertheless, for all wind conditions, the dispersion of the Doppler shift is always not null and for a wind speed of 10 $\mathrm{m} \cdot \mathrm{s}^{-1}$ the ground cells location shift can reach 50 m whatever the wind direction and the incidence angle.

It should be noted that the aforementioned conclusions have considered the mean Doppler shift and its dispersion value, and they should be moderated at least for the cases of null mean Doppler shifts. Indeed, in that case, we can consider that the dispersion value of the shift is a possible value that does not systematically occur and that the shift in the ground cells location is random. We can anticipate that the impact of this random shift on the ground cells location is an additional noise on the range and, hence, the ocean height estimate. We recommend that further assessment of the impact of the aforementioned findings on the present algorithms being designed for SWOT mission be performed.

In the case of the nadir Doppler altimetry in Ku-band as for CryoSat-2, Sentinel-3, and Jason-6, the incidence angle is zero; and the mean value of the Doppler shift is always zero. However, the dispersion value of the Doppler shift is, again, not null as for the SWOT mission case. For the case of Ku-band, the dispersion term is of about 40 Hz inducing a possible ground cell shift of approximately 50 m. This may be again not negligible and could increase the ocean height estimation noise. This should be carefully analyzed in the future.

Another conclusion of the present study is that the instantaneous residual Doppler shift distribution at low incidence can be used as a proxy of wind speed through its dispersion parameter rather than its centroid frequency, whereas the wind direction can be, in principle, estimated from its azimuthal variations. While this is certainly not the optimal way to estimate the wind vector, as compared with conventional scatterometers, this information could be used in complement to another sensor. For example, this supports the concept of azimuthally scanning radars in the range of 0°–15° of incidence, such as the SWIM instrument of the CFOSAT mission [34], which has been primarily devised for wave spectra estimation but could be also used in an upgraded coherent version for simultaneous wind estimation. Another interesting potential application is the estimation of the wind vector in extreme weather conditions. We did not push the model to very high wind speed, at which the spectral surface models, as well as the PO/GO scattering models, become questionable. However, it is known that the altimeter cross section remains sensitive to wind speed even by strong sea states. If the observed trends remain true at higher wind speed, the Doppler-based wind estimation at low incidence could be a valuable tool for wind vector estimation in high wind conditions. As to the surface current, its component along the radar direction at low incidence is too weak to be estimated from a Doppler shift. However, even at large incidences, where its effect is larger, the contribution of surface current to the Doppler shift is drowned in the Doppler anomaly induced by wave motion, which is the dominant contribution. Hence, the elimination of this Doppler anomaly is a first necessary step in view of any estimation of the surface current. For this, it might be interesting to combine multiple sensors at low and high incidences to better characterize the long waves and their Doppler anomaly.

VII. Conclusion

We have investigated the decorrelation time and the instantaneous residual Doppler shift distribution of the sea surface backscattered signal in the framework of the PO and GO at low incidence. A simple expression has been found for the decorrelation time as a function of the main sea state parameters (peak wavenumber and significant wave height), in excellent agreement with the rare data available in the literature. For the SWOT mission, the decorrelation time is consistent with the multilook averaging process. In the framework of the PO, we have proposed a TDE for the instantaneous residual Doppler shift distribution due to wave motion resulting in a simple analytic expression in terms of a nonstandardized Student's t-distribution and the statistical parameters of the surface. The limitation of the TDE, namely, the inability to separate positive and negative Doppler shifts, is overcome to produce a full two-sided Doppler spectrum. The evolution of the mean and dispersion of the Doppler shift has been investigated with respect to the sea states and the scattering angles. The mean Doppler shift has a weak sensitivity to wind speed but its dispersion dramatically increases with the latter, suggesting that the width of the Doppler shift distribution is a better proxy than its mean value for wind speed estimation at low incidence. The situation is opposite when it comes to the influence of the scattering geometry as the mean Doppler frequency mainly depends on the scattering angles, whereas the dispersion parameter mainly depends on the surface roughness. We have further shown that the mean Doppler frequency follows a sinusoidal variation in azimuth with respect to the wind direction, which could be used to devise a robust estimator of its direction. The influence of additional surface currents has been evaluated. Their impact on the mean Doppler shift cannot be separated from the wave-induced Doppler anomaly unless the latter is known and accurately compensated by some other means. However, even in this case, a systematic inversion seems out of reach as the relative contribution of the surface current to the mean Doppler shift is small, whereas the dispersion of the wave-induced Doppler shift is large. Finally, it has been recommended that the derived distribution of Doppler shift be further considered in the SWOT mission to further assess the impact on the estimated parameters and possibly improve the algorithms accordingly.

Appendix A

In the limit of short radar-wavelength the coherent term $e^{-Q_z^2 \rho_0}$ in integral (8) vanishes and the spatiotemporal correlation function of the surface (ρ) can be approximated by its

$$C_{\mathrm{GO}}(t) = \overbrace{e^{-\frac{Q_z^2}{2}\left[s_{tt}^2 - \frac{s_{yy}^2 s_{xt}^2 - 2s_{xy}^2 s_{xt} s_{yt} + s_{xx}^2 s_{yt}^2}{\Sigma^2}\right] t^2}}^{T_{\mathrm{GO}}(t)\ (13)} \overbrace{e^{-i[Q_{Hx}x_0(t) + Q_{Hy}y_0(t)]}}^{\mathbb{M}_{\mathrm{GO}}(t)\ (16)} \times \underbrace{\frac{1}{\pi}\frac{|\mathbb{K}|^2}{Q_z^2}\int_{-\infty}^{\infty}\int_{-\infty}^{\infty} e^{-i[Q_{Hx}x + Q_{Hy}y]} e^{-\frac{Q_z^2}{2}\left[s_{xx}^2 x^2 + 2s_{xy}^2 xy + s_{yy}^2 y^2\right]} dxdy}_{\sigma_{\mathrm{GO}}^0\ (10)} \quad (51)$$

second-order Taylor expansion about the origin (the dependence to the wind direction ϕ_w is implicit in the following expressions):

$$\rho(0,0,0) - \rho(x,y,t) \simeq s_{xx}^2 \frac{x^2}{2} - s_{xt} xt + s_{xy}^2 xy - s_{yt} yt + s_{yy}^2 \frac{y^2}{2} \quad (49)$$

where the coefficients are defined by (11) and (15). Denoting Q_{Hx} andQ_{Hy} the projections of the horizontal component of the Ewald vector ($\mathbf{Q_H}$) on the x- and y-axis, respectively, this leads to the following approximation of the correlation integral:

$$C_{\mathrm{GO}}(t) = \frac{1}{\pi}\frac{|\mathcal{K}|^2}{Q_z^2} e^{-\frac{Q_z^2}{2} s_{tt}^2 t^2} \int_{-\infty}^{\infty}\int_{-\infty}^{\infty} e^{-i[Q_{Hx}x + Q_{Hy}y]} \times \cdots$$

$$\cdots e^{-\frac{Q_z^2}{2}\left[s_{xx}^2 x^2 - 2s_{xt} xt + 2s_{xy}^2 xy - 2s_{yt} yt + s_{yy}^2 y^2\right]} dxdy. \quad (50)$$

Using the standard formula for the Fourier transform of a noncentered 2-D Gaussian function, we obtain, (51) shown at the top of the page. leading to expression (9).

ACKNOWLEDGMENT

The authors would like to thank M. Saillard for useful comments.

REFERENCES

[1] D. R. Thompson, "Calculation of microwave Doppler spectra from the ocean surface with a time-dependent composite model," in *Radar Scattering from Modulated Wind Waves*. New York, NY, USA: Springer-Verlag, 1989, pp. 27–40.

[2] W. J. Plant, "A model for microwave Doppler sea return at high incidence angles: Bragg scattering from bound, tilted waves," *J. Geophys. Res., Oceans*, vol. 102, no. C9, pp. 21 131–21 146, 1997.

[3] V. U. Zavorotny and A. G. Voronovich, "Two-scale model and ocean radar Doppler spectra at moderate-and low-grazing angles," *IEEE Trans. Antennas Propag.*, vol. 46, no. 1, pp. 84–92, Jan. 1998.

[4] R. Romeiser and D. Thompson, "Numerical study on the along-track interferometric radar imaging mechanism of oceanic surface currents," *IEEE Trans. Geosci. Remote Sens.*, vol. 38, no. 1, pp. 446–458, Jan. 2000.

[5] B. Chapron, F. Collard, and F. Ardhuin, "Direct measurements of ocean surface velocity from space: Interpretation and validation," *J. Geophys. Res., Oceans*, vol. 110, no. C7, pp. 76–92, Jul. 2005.

[6] A. A. Mouche, B. Chapron, N. Reul, and F. Collard, "Predicted Doppler shifts induced by ocean surface wave displacements using asymptotic electromagnetic wave scattering theories," *Waves Random Complex Media*, vol. 18, pp. 185–196, 2008.

[7] F. Nouguier, C.-A. Guérin, and G. Soriano, "Analytical techniques for the Doppler signature of sea surfaces in the microwave regime—I: Linear surfaces," *IEEE Trans. Geosci. Remote Sens.*, vol. 49, no. 12, pp. 4856–4864, Dec. 2011.

[8] F. Nouguier, C.-A. Guérin, and G. Soriano, "Analytical techniques for the Doppler signature of sea surfaces in the microwave regime—II: Nonlinear surfaces," *IEEE Trans. Geosci. Remote Sens.*, vol. 49, no. 12, pp. 4920–4927, Dec. 2011.

[9] X. Li and X. Xu, "Scattering and Doppler spectral analysis for two-dimensional linear and nonlinear sea surfaces," *IEEE Trans. Geosci. Remote Sens.*, vol. 49, no. 2, pp. 603–611, Feb. 2011.

[10] Y. Wang, Y. Zhang, M. He, and C. Zhao, "Doppler spectra of microwave scattering fields from nonlinear oceanic surface at moderate-and low-grazing angles," *IEEE Trans. Geosci. Remote Sens.*, vol. 50, no. 4, pp. 1104–1116, Apr. 2012.

[11] F. Fois, P. Hoogeboom, F. Le Chevalier, and A. Stoffelen, "An analytical model for the description of the full-polarimetric sea surface Doppler signature," *J. Geophys. Res., Oceans*, vol. 120, no. 2, pp. 988–1015, 2015. doi: http://dx.doi.org/10.1002/2014JC010589.

[12] J. V. Toporkov and G. S. Brown, "Numerical simulations of scattering from time-varying, randomly rough surfaces," *IEEE Trans. Geosci. Remote Sens.*, vol. 38, no. 4, pp. 1616–1624, Jul. 2000.

[13] J. Johnson and R. Burkholder, "Coupled canonical grid/discrete dipole approach for computing scattering from objects above or below a rough interface," *IEEE Trans. Geosci. Remote Sens.*, vol. 39, no. 6, pp. 1214–1220, Jun. 2001.

[14] A. R. Hayslip, J. T. Johnson, and G. R. Baker, "Further numerical studies of backscattering from time evolving non-linear sea surfaces," *IEEE Trans. Geosci. Remote Sens.*, vol. 41, no. 10, pp. 2287–2293, Oct. 2003.

[15] G. Soriano, M. Joelson, and M. Saillard, "Doppler spectra from a two-dimensional ocean surface at l-band," *IEEE Trans. Geosci. Remote Sens.*, vol. 44, no. 9, pp. 2430–2437, Sep. 2006.

[16] J. V. Toporkov and M. A. Sletten, "Statistical properties of low-grazing range-resolved sea surface backscatter generated through two-dimensional direct numerical simulations," *IEEE Trans. Geosci. Remote Sens.*, vol. 45, no. 5, pp. 1181–1197, May 2007.

[17] C.-S. Chae and J. T. Johnson, "A study of sea surface range-resolved Doppler spectra using numerically simulated low-grazing-angle backscatter data," *IEEE Trans. Geosci. Remote Sens.*, vol. 47, no. 6, pp. 3452–3460, Jun. 2013.

[18] D. Miret, G. Soriano, F. Nouguier, P. Forget, M. Saillard, and C.-A. Guérin, "Sea surface microwave scattering at extreme grazing angle: numerical investigation of the Doppler shift," *IEEE Trans. Geosci. Remote Sens.*, vol. 52, no. 11, pp. 7120–7129, Nov. 2014.

[19] M. H. Sharqawy, J. H. Lienhard V, and S. M. Zubair, "Thermophysical properties of seawater: A review of existing correlations and data," *Desalination Water Treat.*, vol. 16, pp. 354–380, Apr. 2010.

[20] T. Elfouahily, B. Chapron, K. Katsaros, and D. Vandemark, "A unified directional spectrum for long and short wind-driven waves," *J. Geophys. Res.*, vol. 102, no. C7, pp. 15 781–15 796, Jul. 1997.

[21] M. S. Longuet-Higgins, D. E. Cartwright, and N. D. Smith, "Observations of the directional spectrum of sea waves using the motions of a floating buoy," in *Ocean Wave Spectra*. Englewood Cliffs, NJ, USA: Prentice-Hall, 1963, pp. 111–136.

[22] W. J. Plant, "A stochastic, multiscale model of microwave backscatter from the ocean," *J. Geophys. Res., Oceans*, vol. 107, no. C9, pp. 3-1–3-21, Sep. 2002. [Online]. Available: http://dx.doi.org/10.1029/2001JC000909

[23] T. Elfouhaily and C.-A. Guérin, "A critical survey of approximate scattering wave theories from random rough surfaces," *Waves Random Complex Media*, vol. 14, no. 4, pp. 1–40, 2004.

[24] P. Beckmann and A. Spizzichino, *The Scattering of Electromagnetic Waves From Rough Surfaces*. Norwood, MA, USA: Artech House, 1987.

[25] R. D. Chapman, B. L. Gotwols, and R. E. Sterner, "On the statistics of the phase of microwave backscatter from the ocean surface," *J. Geophys. Res., Oceans*, vol. 99, no. C8, pp. 16 293–16 301, 1994. doi: http://dx.doi.org/10.1029/94JC01111.

[26] S. Madsen, "Estimating the Doppler centroid of SAR data," *IEEE Trans. Aerosp. Electron. Syst.*, vol. 25, no. 2, pp. 134–140, Mar. 1989.

[27] R. Baxley, B. Walkenhorst, and G. Acosta-Marum, "Complex Gaussian ratio distribution with applications for error rate calculation in fading channels with imperfect CSI," in *Proc. IEEE GLOBECOM*, Dec. 2010, pp. 1–5.

[28] A. A. Mouche *et al.*, "On the use of Doppler shift for sea surface wind retrieval from SAR," *IEEE Trans. Geosci. Remote Sens.*, vol. 50, no. 7, pp. 2901–2909, Jul. 2012.
[29] K. F. Dagestad *et al.*, "Wind retrieval from synthetic aperture Radar—An overview," Eur. Space Agency, ESA, Paris, France, 2013.
[30] A. C. H. Martin, C. Gommenginger, J. Marquez, S. Doody, V. Navarro, and C. Buck, "Wind-wave-induced velocity in ATI SAR ocean surface currents: First experimental evidence from an airborne campaign," *J. Geophys. Res., Oceans*, vol. 121, no. 3, p. 1640–1653, 2016.
[31] P. Forget, M. Saillard, C.-A. Guérin, J. Testud, and E. L. Bouar, "On the use of x-band weather radar for wind field retrieval in coastal zone," *J. Atmosp. Ocean. Technol.*, vol. 33, no. 5, pp. 899–917, May 2016.
[32] Z. Guerraou, S. Angelliaume, L. Rosenberg, and C.-A. Guérin, "Investigation of azimuthal variations from x-band medium grazing angle sea clutter," *IEEE Trans. Geosci. Remote Sens.*, vol. 54, no. 10, pp. 6110–6118, Oct. 2016.
[33] M. Durand, L. L. Fu, D. P. Lettenmaier, D. E. Alsdorf, E. Rodriguez, and D. Esteban-Fernandez, "The surface water and ocean topography mission: Observing terrestrial surface water and oceanic submesoscale eddies," *Proc. IEEE*, vol. 98, no. 5, pp. 766–779, May 2010.
[34] C. Tison *et al.*, "Directional wave spectrum estimation by swim instrument on CFOSAT," in *Proc. IEEE Int. Geosci. Remote Sens. Symp.*, Jul. 2009, vol. 5, pp. V-312–V-315.

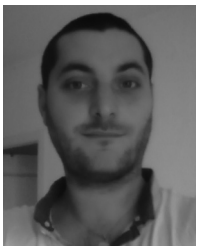

Olivier Boisot was born in Toulon, France, in 1987. He received the M.S. degree in physics and engineering sciences and the Ph.D. degree in physics from the University of Toulon, La Garde, France, in 2012, respectively 2015.

He was with the Mediterranean Institute of Oceanography, University of Toulon, La Garde, France, the Centre National d'Études Spatiales (CNES), Toulouse, France, and Collecte Localisation Satellite (CLS), Toulouse, France, on electromagnetic scattering modelization from rough surfaces and its applications to the Surface Water and Ocean Topography mission. He is currently a Postdoctoral Fellow with the Office National d'Études et de Recherches Aéspatiales (ONERA), Salon-de-Provence, France, and is working on the detection and characterization of chemical products and oil on the ocean surface from synthetic aperture radar measurements in microwave bands.

Laïba Amarouche, photograph and biography not available at the time of publication.

Jean-Claude Lalaurie

Since 1991, he has been an Engineer with the Centre National d'Études Spatiales (CNES) and started his career in microwave instrument design and development [MMIC components for radio communication equipment and synthetic aperture radar (SAR) systems]. In 1999, he started specializing in electric and magnetic field instruments for plasma characterization. He was involved in the development of several instruments, including Demeter, Venus Express, and SWARM. Since 2010, he has been on water surface backscattering characterization, interferometric SAR height bias estimation, and acquisition of near-field and airborne Ka-band data in the framework of the Surface Water and Ocean Topography project.

Charles-Antoine Guérin received the B.Eng. degree from the Ecole Nationale Supérieure de l'Aéronautique et de l'Espace, Toulouse, France, in 1994 and the Ph.D. degree in theoretical physics from the University of Aix-Marseille, Marseille, France, in 1998.

He is currently a Professor and Researcher with the Mediterranean Institute of Oceanography, University of Toulon, La Garde, France. He specializes in ocean remote sensing.